Pergamon

Int. J. Heat Mass Transfer. Vol. 41, Nos 6–7, pp. 899–914, 1998

Printed in Great Britain
0017–9310/98 $19.00 + 0.00

PII: S0017–9310(97)00168–3

Experimental studies of heat transfer and fluid flow across corrugated–undulated heat exchanger surfaces

J. A. STASIEK

Technical University of Gdansk, Faculty of Mechanical Engineering, G. Narutowicza 11/12, 80-952 Gdansk, Poland

(*Received* 28 *February* 1997 *and in final form* 28 *May* 1997)

Abstract—True-colour image processing of liquid crystal (LC) images has been established as a new powerful experimental technique to yield full-field measurements of temperature and heat transfer coefficient distributions. In this study the LC technique was developed successfully and applied to a study of six element-shapes of rotary air heat preheaters are used extensively in power stations. A complete mapping of temperature, heat transfer coefficient and pressure drop was obtained for all of them at every angle and Reynolds number required. The measuring technique comprising the use of LC flexible sheets and true-colour processing may also be used for a great variety of applications and should be of considerable use in improving the design of all types of compact heat exchanger. © 1997 Elsevier Science Ltd.

INTRODUCTION

Rotary air heaters [1] are used extensively in power stations for the final recovery of heat from the combustion products. The importance of reliable thermohydraulic performance of plate heat exchangers does not require any demonstrations. Improvements in their flow and thermal characteristics would substantially reduce fuel costs. The main requirements for an air heater are high heater transfer rates, low pressure losses and low sensitivity to fouling. These depend mainly on the heat transfer element geometrical design. Various element shapes and arrangements have been developed from experimental studies of overall heat transfer and pressure loss coefficients, but the available data is insufficient for a full optimisation study. These considerations led to the execution of a comprehensive experimental and analytical investigation at City University supported by PowerGen U.K. [2]. The main aims of this study were:

(i) to determine the flow patterns and local heat transfer coefficients in the passages formed between symmetrical crossed corrugated (CC) surfaces. By this means regions of high wall shear stress and mechanical energy dissipation were identified and local 'hot' and 'cold' spots located to aid the design of high efficiency surfaces;

(ii) to investigate the dependence of average heat transfer coefficients and pressure drops on the geometrical parameters and Reynolds number;

(iii) to test and validate alternative computational approaches against well controlled experimental data.

The experimental work was mainly concerned with the measurement of local Nusselt numbers by digital of liquid crystals colour images (liquid crystal thermography—LCT) [2]. Also, the wall pressure distribution was measured with pressure tappings, and preliminary investigation of the flow field was conducted by particle image velocimetry (PIV). The analytical studies were based mainly on three-dimensional flow simulations using the U.K. Harwell Laboratory CFD code, FLOW3D (Release 2) suitably adapted [3]. Predictions were made both for laminar and turbulent flow conditions. In the latter case, various turbulence models were used, including direct and large-eddy simulations (LES) with different boundary conditions. Experimental and numerical results were critically compared and were also assessed against bulk performance data and laboratory results available from the literature. The main numerical and experimental results from previous investigations have been documented in a series of confidential reports [2], they have also been partially published, in Refs [4–6].

Success with these studies has led to continuation of the work with an investigation of the more complex 'corrugated–undulated' (CU) surfaces shown in Fig. 5. Here for the first time, the local Nusselt number distribution is measured by the process of image combination techniques (ICT). Using the image combination technique features of Global Lab. Color software of Data Translation Inc. [7] false colour image of Nusselt number distribution also was developed. However, the main purpose of the investigation was to determine the distribution of temperature and local heat transfer coefficient on six specified shapes of corrugated–undulated (CU) heat exchanger elements and how CU heat transfer and pressure drop vary without angle shape factors and Reynolds number.

NOMENCLATURE

A	flow cross-section
a, b	constant of equation (13)
D_h	hydraulic diameter
f	friction factor or fluid
H	corrugation height (external)
H_i	corrugation height (internal)
h	heat transfer coefficient
h_l	local heat transfer coefficient
k_t	thermal conductivity
L	length of the corrugation–undulation structure
N	number of ducts
Nu	Nusselt number
P	pressure or corrugation pitch
ΔP	pressure drop
q	heat flux
Re	Reynolds number
r	radius or pixels ratio
S	parameter length of the structure or the wetted parameters of the corrugated and undulated duct
T	temperature
U	air velocity
V	volumetric flow rate.

Greek symbols

δ	wall thickness
ν	kinematic viscosity
ρ	density
ϕ	angle of inclination.

Subscripts

a	air temperature
b	water bath temperature
c	corrugation structure
l	local or liquid crystal values
n	normal value
o	reference point
u	undulation structure.

Additional aims were:

(i) to introduce colour digital processing of liquid crystal images to yield full-field measurements of temperature and the surface distribution of heat transfer coefficients;

(ii) to establish a new false colour combination technique for local heat transfer coefficient distribution. This involves colour scale representation of a sequence of video images into a single image using the Global Lab software of Data Translation Inc. [7];

(iii) to obtain average Nusselt number as a weighted mean value of the local Nusselt numbers and the hue ratio coefficient where the hue ratio coefficient is the ratio of number of pixels for the hue range considered: total number of pixels and hue is one of the colour space attributes.

LIQUID CRYSTALS AND IMAGE PROCESSING

Liquid crystals: a background survey

In 1888 an Austrian botanist, Fredrich Reinitzer [8] observed that certain organic compounds appeared to possess two melting points, an initial m.p. at which the solid phase turned to a cloudy and a second m.p. at which the cloudy liquid turned clear. Further research revealed that an intermediate phase or 'mesophase' did indeed exist between the pure solid and pure liquid phase of some organic compounds. Reinitzer termed this phase as 'liquid crystal', an appropriate designation when one considers that the material exhibits the fluidity of a liquid while maintaining the characteristic of the anisotropic, ordered structure of a crystalline solid. The mesophases have been classified as nematic, cholesteric and smectic. However, from a structural viewpoint it can be argued that there are only two basic types of liquid crystal: chiral-nematic and smectic; with cholesteric being regarded as a special kind of nematic. In the present work, no attempt was made to study the detail of the molecular structure of liquid crystals. Excellent papers on this aspect of liquid technology have been published by Brown and Shaw [9], Fergason [10], Stephan and Straley [11] and more recently by Jones *et al.* [12], Parsley [13] and the manufacturers' handbooks [14, 15]. Nevertheless, chiral-nematic liquid crystals, are extremely optically active and react to changes in temperature and/or shear by changing colour. This peculiar optical behaviour is brought about by the molecular structure of these materials: the molecules are thin, rod-like structures which, in the non-isotropic liquid (i.e. crystalline) form, have their long axis aligned in a certain direction. In the smectic phase the molecules form layers, each with their long axis pointing in the same direction; this phase is optically inactive. The ability to change colour by changing temperature and/or shearing is due to Bragg-like scattering of incident white light caused by the helical structure of the chiral-nematic phase. Changing the temperature or the action of shear alters the pitch of the helix and hence the reflected wave length: in effect when illuminated with white light the liquid crystal layer changes colour. Hence, upon heating, the liquid crystals will change

from the optically inactive (colourless) smectic phase through the visible spectrum from red to violet and then turn colourless again at high temperatures as the isotropic liquid phase is formed. The effect (illustrated in Fig. 1) is reversible which, in practical terms, means that a single application of liquid crystals to a model can be used repeatedly (usually until the coating film is oblated or otherwise damaged).

Over a known, reproducible range of temperature, the 'even temperature range', the cholesteric liquid crystal will progressively exhibit all colours of the visible spectrum as it is heated through the event temperature range. Both the colour play interval (that is, the range of temperature over which a certain colour is visible) and the event temperature range of a liquid crystal can be selected by adjusting its composition, and materials are available with event temperature from -30 to 120°C and with colour play bands from 0.5 to 20°C although not all combinations exist of event temperature and colour play band widths. The types of material to be specified for a given task depends on the type of image interpretation technique to be used.

True-colour image processing technique

There are several commercial packages of hardware and software available which will digitise a video image from either black and white or colour cameras and store individual frames pixel by pixel in arrays. Three separate arrays are used to store a colour image, one for the red, green and blue signal components. Also, three styles of camera have been used: NTSC composite (the usual home video camera), CCD (change-coupled device) and CID (charge injected device). According to Akino *et al.* [16], Moffat [17] and Jones *et al.* [12] there are four broad classes of image interpretation techniques available: human observers, multiple narrow-band spectral intensity image processing system, multiple linear regression method and true-colour or chromaticity based image processing systems.

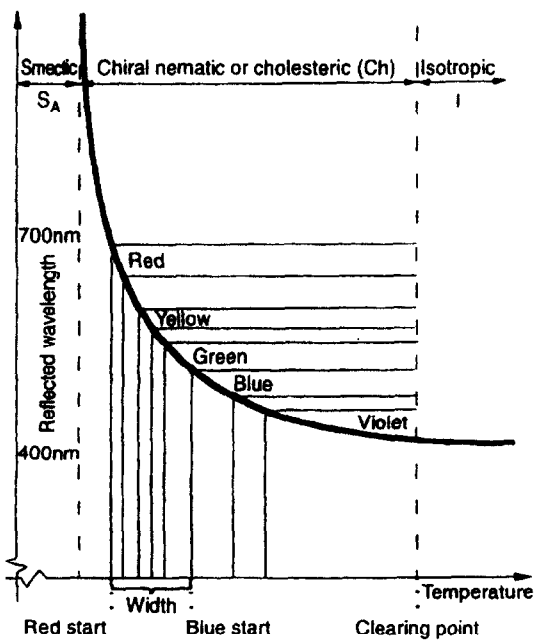

Fig. 1. Typical liquid crystal response.

Human observers can interpret liquid crystal images by direct visual inspection of colour photographs or tape recorded video images, usually using narrow-band points. Calibrations for such use are generally limited to identifying the temperature associated with a particular colour often the red or the yellow–green colour near the centre of the colour-play band. The uncertainty associated with direct visual inspection is about 1/3 the colour-play band-width, given an observer with normal colour vision and a little experience, Moffat [17], or about ± 0.2–0.5°C, depending on the band width.

The second and third methods are based on the interferential optical filters with narrow band-play characteristics of transmittance, through which equally coloured regions can be extracted. Akino *et al.* [16] developed a multiple narrow-band spectral intensity interpreter using a set of 18 narrow band-pass filters, whose central wavelengths were from 400 to 750 nm, and the full width of the half maximum (FWHM) of the filters were less than 10 nm. The behaviour of liquid crystals can be interpreted in terms of the variation of intensity with wavelength, at a given temperature instead of the variation of dominant with hue temperature. Good results were obtained, by these same authors [16], using sets of three filters, chosen considering the spectral characteristics of the microencapsulated liquid crystals used in conjunction with the lighting. Temperature was expressed as a linear function of the intensities passed by the three filters (red, green and blue). With three filters, four coefficients are required, and those were found by calibration. The authors quote an uncertainty of ± 0.1°C for the method and a spatial resolution of 1 mm.

In the fourth method Hollingsworth *et al.* [18] approached the image interpretation problem from the standpoint of standard colour video practice, electing to work with the relationship between the dominant hue and temperature as the primary function, rather than the intensity distribution as a function of wavelength. The relative functions of red, green and blue (RGB) determine perceived colour, and also can be treated as the independent variables with which to represent the colour numerically. In this method a displayed RGB image is immediately perceived by a user as exhibiting three distinct attributes (HSI): hue—the spectral colours present; saturation—how deep or faded the colour appear to be; and intensity—the edge information or what would be seen if a black-and-white version of the image were displayed (hence,

only intensity is available from a monochrome system).

The uncertainty of true-colour interpreters using a wide-band liquid crystals is of the same order as the uncertainty resulting from human observers using narrow-band materials. It depends on the pixel-to-pixel uniformity of the applied paint and on the size of the area averaged by the interpreter [17, 18]. Many image processing operations developed for processing grey-level (intensity) images can be readily applied to HSI colour images. Building on grey-scale image processing hardware and software, Data Translation Inc. [7] has produced a 512×512 pixels $\times 8$ bit (256 grey levels) colour frame-grabber board for PC/ATs.

A schematic view of such an image processing system (developed by the author) is shown in Fig. 2. The two-dimensional temperature distribution is determined using RGB video-camera, IBM 386 Personal Computer AT, HSI Colour Frame Grabber DT 2871 and Auxiliary Frame Processor DT 2858. As shown, the chart is also for an RGB video-recorder (JVC-S6O5E), includes a Time Based Corrector VT 3000 and KM-V7EK RGB converter. New chart with JVC-S6O5E as the terminal makes it possible for presentation tapes to be loaded cued and played exactly on schedule with all operation handled by the computer. This can even be done with unattended presentation via a modem. For fast and transit method, accurate location of specific scenes or edit points JVC-S6O5E is provided with a convenient, easy-to-use search dial. A time base corrector (TBC) controls times tracking systems and easy identification colour-coded images.

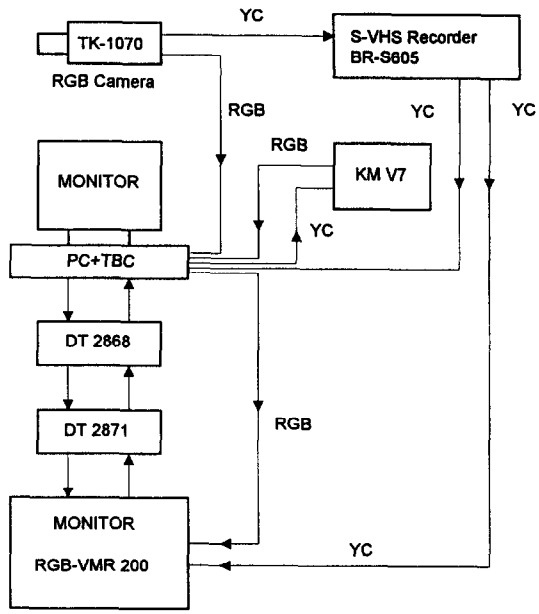

Fig. 2. Block diagram of the true-colour image processing system.

Calibration of liquid crystals

Before the execution of a thermal or flow visualisation experiment, we should recognise the characteristics of the overall combination of the TLC, the light source, the optical and camera system (ordinary, CCD black and white or RGB colour camera), and make a rational plan for the total measurement system. The relationship between the temperature of the crystal and the measured hue of the reflected light defines the calibration curve for the liquid crystal. The result is a curve relating the hue of the reflected light to the surface temperature. A known temperature distribution exists on a 'calibration plate' (brass plate) to which is attached the liquid crystal layer. The distribution of the colour component pattern on the liquid crystal layer was measured by RGB colour camera and a series of images at different temperatures defines the calibration. A representative calibration curve including hue and temperature distribution along plate is shown in Fig. 3 [2, 14].

In this particular experiment uncertainty was estimated as about ± 0.05°C by considering only the section of the surface used in the experiment, spanwise non-uniformities in hue, value are minimised. Also the isotherms of the yellow–green colour band are recorded as narrow as 0.1°C. Approximately half this band width can be detected [17].

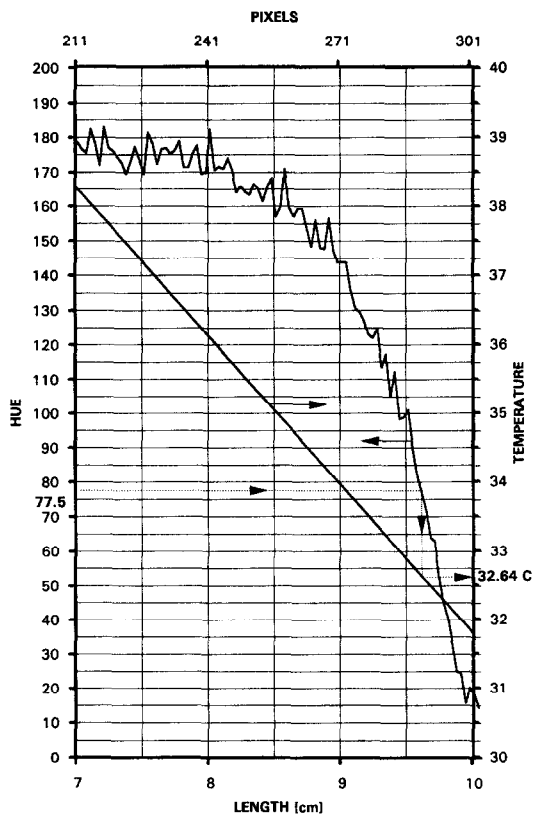

Fig. 3. Representative calibration curve—hue and temperature distribution along the test plate.

EXPERIMENTAL ARRANGEMENT AND MEASUREMENT

Design and construction of the wind tunnel

The experimental study was carried out using an open low speed wind tunnel (described in Refs [2, 4]) consisting of entrance section with fan and heater, large settling chambers with diffusing screen and honeycomb and then mapping and working sections. Air is drawn through the tunnel using a fan able to give Reynolds numbers of between 500 and 10^4 and the heaters can provide an air temperature, T_f, between 25 and 60°C. The major construction material of the wind tunnel is perspex. Local and mean velocity are measured using conventional Pitot tubes and DISA hot-wires velocity, probe.

The wind tunnel is instrumented with copper–constantan (type T) thermocouples and resistance thermometer so that the surface, water bath behind the liquid crystal and PVC surface, and air can be measured and controlled by a variac control system. The alternative effects of constant wall temperature or con-

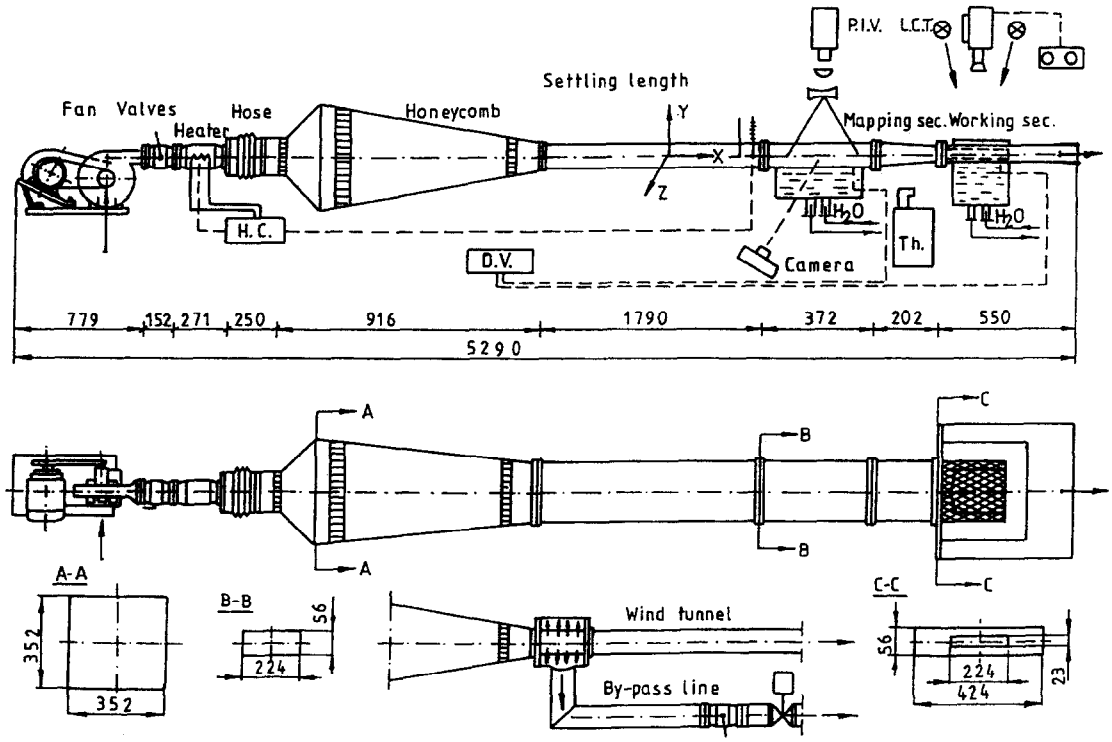

Fig. 4. Open low-speed wind tunnel with extension (instead of working section) containing corrugated–undulated section and an upper constant temperature water bath.

Table 1. Dimensions of corrugated–undulated geometries tested

Geometry	P [mm]	H [mm]	H_i [mm]	P/H	P/H_i	S [mm]	δ [mm]	D_h [mm]
Corrugated plate CP	22.60	13.98	13.13	1.62	1.72	37.0	0.85	↓
Undulated standard US	21.87	4.52	3.65	4.84	6.00	23.1	0.87	12.09
Undulated plate UH1	21.87	6.07	5.20	3.60	4.20	22.5	0.87	13.00
Undulated plate UH2	21.87	3.37	2.50	6.49	8.75	24.0	0.87	11.40
Undulated plate UP1	26.2	4.52	3.65	5.8	7.18	27.0	0.87	12.13
Undulated plate UP2	17.5	4.52	3.65	3.87	4.79	29.0	0.87	9.88
Undulated plate UCS	32.0	8.8	8.0	3.64	4.0	37.0	0.80	14.6

stant heat flux boundary conditions are obtained using a water bath, while the temperature can be controlled with a thermostat capable of establishing and maintaining temperature to within ± 0.01°C accuracy. The facility was successively modified by designing a new end portion, allowing for larger and more flexible working sections consisting of corrugated–undulated (CU) heat transfer elements; this is shown in Fig. 4. Photographs are taken using a standard camera and RGB video-camera, respectively.

Duct geometry and thermal hydraulic properties

The geometry of corrugated–undulated (CU) heat transfer elements is shown in greater detail in Fig. 5.

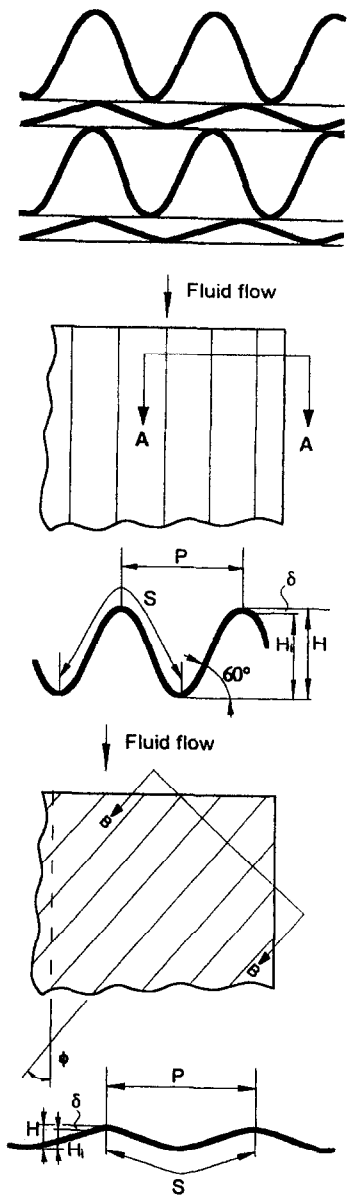

Fig. 5. A general view of a corrugated–undulated heat transfer element.

Both sides of the working (test) section (CU) can be closed or open and void into a large rectangular box, 80×570 mm in cross-section and 700 mm long. Plates with undulation inclination angles $\phi = 20$, 30, 50 and 70° relative to the main flow direction (or the corrugation ducts) were tested. The main geometrical parameters of the corrugation–undulation (CU) test section used at City University are summarised in Table 1. Note that this experimental study was carried out for a *closed working section*—it is different from what was done for the crossed-corrugated geometry [2]. Therefore, the reference velocity U of the fluid in the corrugated/undulated ducts is defined as the volumetric flow rate in the unitary cell (i.e. the volumetric flow rate per couple of ducts), divided by the cross-sectional area A_n given by equation (1):

$$A_n = A_{nc} + A_{nu} \tag{1}$$

where

$$A_{nc} = \left(\frac{P_c H_c - S_c \delta_c}{2}\right) N_c \tag{2}$$

$$A_{nu} = \left(\frac{P_u H_u - S_u \delta_u}{2}\right) N_u \tag{3}$$

in which N_c and N_u are number of ducts, and A_{nc} and A_{nu} are the cross-sectional areas of the corrugated and undulated plates, respectively, normal to the duct's axes, of course, the equivalent (hydraulic) diameter of the unitary cell (and the whole heat exchange matrix) as follows:

$$D_h = \frac{4A_n}{(S_c + S_u)} \tag{4}$$

where $(S_c + S_u)$ are the 'wetted' parameters of the corrugated and undulated plate, respectively. As usual, the reference velocity U of the fluid in the corrugated/undulated ducts is defined as the volumetric flow rate divided by the cross-section area given by equation (1). It is also equal to the velocity of the incoming flow just upstream of the exchanger, divided by the 'porosity' of the heat exchange matrix (which can be defined as the ratio of internal volume to total volume) and can be easily derived from equation (5).

$$U = \frac{U_0 \cdot A_0}{A_n} \tag{5}$$

where U_0 and A_0 are average velocity and cross-sectional area, respectively where conventional Pitot tubes and DISA hot-wires velocity probe were mounted. The most relevant performance parameters of the heat exchange matrix are the pressure drop per unit length and the heat transfer coefficients. The wall pressure distribution was measured using eight pressure tappings ~ 0.5 mm in diameter, located along the 'crests' of the top corrugated plate in conjunction with a micro-manometer. The equivalent friction coefficient

f was computed by averaging over 210 mm length of the CU structure.

PERFORMANCE PARAMETERS AND EXPERIMENTAL RESULTS

Heat transfer

The heat transfer coefficient is a defined quantity, calculated from the surface heat flux and the difference between the surface temperature and some agreed reference temperature. This is usually the far field temperature, the mixed mean temperature or the adiabatic surface temperature. In the experiments described here, liquid crystals were used to determine the distribution of surface temperature and heat flux. This allows evaluation of the local heat transfer coefficient and Nusselt number. The temperature recorded from the liquid crystal sheet was held at red for human observation, to ease viewing, and at yellow–green for image processing.

The local convective heat transfer coefficient h_l is derived from the fact that the conductive heat flux q_k in either working section is equal to the convective heat flux from air to the surface in the steady-state:

$$h_l = \frac{k_t (T_l - T_b)}{\delta_t (T_a - T_l)} \tag{6}$$

where k_t is the mean conductivity of the liquid crystal package and plate, δ_t is the thickness of the liquid crystal package and plate, T_l is the temperature of surface (liquid crystal yellow–green isotherm temperature), T_b is the temperature of plate from water side and T_a is the temperature of air.

The experimental results are presented in terms of a local Nusselt number:

$$Nu_l = h_l D_h / k_a \tag{7}$$

where k_a is the conductivity of the air.

With the temperature difference between the air and liquid crystal isotherm fixed, different heat transfer coefficient (Nusselt number) contours are determined by varying the heat flux values. The contours of constant heat transfer coefficient are not directly equivalent to the isotherms, as measured from the photograph or images. They are determined after taking into account thermal conduction in the plate, radiation from the surface and other corrections, the most important of which is the lateral conduction. This correction is typically about 4% of the net flux [2, 19].

The liquid crystal colour temperature T_l is 32.1°C, some 13.23°C below the air temperature (T_a = 45.33°C) for these experiments. Ten to sixteen isotherms (each corresponding to a different heat flux) are photographed by RGB camera to record the local contours under an oblique Reynolds number. The location on each isotherm was originally digitised following projection of the photographic image onto the digitising pad. Now, however, a new procedure has been developed that involves colour scale representation of the several video images of the heat transfer coefficient distribution into a single image using the Global Lab software of Data Translation Inc. [7] as described in ref. [2].

Average Nusselt numbers are estimated as weighted mean values of the local Nusselt numbers obtained from the relationship:

$$Nu_{av} = \frac{\sum_{i=1}^{n} Nu_i r_i}{\sum_{i=1}^{n} r_i} \tag{8}$$

where r_i is the hue ratio coefficient (ratio of number of pixels for the hue range considered).

By using equations (6)–(8) and the image combination technique capabilities of Global Lab Color, colour images like that in Fig. 10 were obtained. This shows the Nusselt number distribution on the corrugated–undulated wall for the central diamond of the CU working reaction. The overall heat transfer results are summarised in Figs 8 and 9.

Pressure drop

As mentioned before, the second most relevant performance parameter of the heat exchange matrix is the pressure drop per unit length. The pressure drop can be made dimensionless by defining the equivalent friction factors coefficient:

$$f = \frac{2\Delta P D_h}{\rho L U^2} \tag{9}$$

in which L is the length of the corrugation/undulation structure in the main flow direction.

The experimental results are summarised in Figs 11 and 12. The equivalent friction coefficient is reported as a function of the undulation angle ϕ and three Reynolds numbers (Re = 1500, 3000 and 10,000). Empirical correlations obtained by least-squares methods are given in Table 2.

DATA REDUCTION AND UNCERTAINTY ANALYSIS

The experiments were carried out for the Reynolds number (Re) range of 1000–10,000. Re was based on the hydraulic diameter [equation (4)] and the average velocity U defined by equation (5). The wall temperature distribution (T_l) was evaluated from the liquid crystal layer by the present methods. The entrance and exit temperature of air were measured directly by thermocouples, from which the mixed-mean-temperature of air (T_a) was found and agree for all experiments. The air properties were evaluated at T_a. The Nusselt number was obtained from equation (7). Equation (7) is valid assuming the lateral heat transfer by conduction along the wall is negligible compared to wall-to-fluid heat transfer; this assump-

Table 2. Function factors correlations

Inclination angle ϕ	Geometry					
	CP/UH1		CP/US		CP/UH2	
	Re-range	*f*-Correlation	*Re*-range	*f*-Correlation	*Re*-range	*f*-Correlation
20°	1500–2700	$f = 1976Re^{-1.28}$	1500–2700	$f = 122Re^{-0.936}$	1300–3000	$f = 26.36Re^{-0.752}$
	2700–10,000	$f = 2.566Re^{-0.439}$	2700–10,000	$f = 3.327Re^{-0.48}$	3000–1000	$f = 2.050Re^{-0.433}$
30°	1500–2700	$f = 1119Re^{-1.18}$	1500–2700	$f = 44Re^{-0.777}$	1300–3000	$f = 26.57Re^{-0.722}$
	2700–10,000	$f = 0.857Re^{-0.272}$	2700–10,000	$f = 1.868Re^{-0.377}$	3000–1000	$f = 2.203Re^{-0.411}$
50°	1500–2700	$f = 2127Re^{-1.18}$	1500–2700	$f = 95.2Re^{-0.83}$	1300–3000	$f = 16.136Re^{-0.635}$
	2700–10,000	$f = 1.879Re^{-0.29}$	2700–10,000	$f = 0.935Re^{-0.245}$	3000–1000	$f = 1.951Re^{-0.371}$
70°	1500–2700	$f = 2376Re^{-1.113}$	1500–2700	$f = 55.72Re^{-0.719}$	1300–3000	$f = 7.88Re^{-0.499}$
	2700–10,000	$f = 1.479Re^{-0.22}$	2700–10,000	$f = 1.879Re^{-0.29}$	3000–1000	$f = 1.502Re^{-0.292}$
	Geometry					
	CP/UP1		CP/UP2		CP/UCS	
20°	1300–3000	$f = 40.27Re^{-0.771}$	1500–3000	$f = 12.0Re^{-0.666}$	1500–2700	$f = 29.8Re^{-0.743}$
	3000–1000	$f = 2.648Re^{-0.431}$	3000–1000	$f = 0.272Re^{-0.193}$	2700–10,000	$f = 2.42Re^{-0.427}$
30°	1300–3000	$f = 30.653Re^{-0.709}$	1500–3000	$f = 3.02Re^{-0.463}$	1500–2700	$f = 119.8Re^{-0.905}$
	3000–1000	$f = 3.503Re^{-0.438}$	3000–1000	$f = 0.603Re^{-0.262}$	2700–10,000	$f = 0.794Re^{-0.270}$
50°	1300–3000	$f = 24.03Re^{-0.626}$	1500–3000	$f = 27.4Re^{-0.695}$	1500–2700	$f = 637Re^{-0.975}$
	3000–1000	$f = 1.929Re^{-0.311}$	3000–1000	$f = 0.98Re^{-0.279}$	2700–10,000	$f = 2.14Re^{-0.297}$
70°	1300–3000	$f = 9.85Re^{-0.454}$	1500–3000	$f = 5.95Re^{-0.464}$	1500–2700	$f = 2042Re^{-1.112}$
	3000–1000	$f = 2.987Re^{-0.305}$	3000–1000	$f = 1.24Re^{-0.268}$	2700–10,000	$f = 1.552Re^{-0.194}$

tion is well satisfied under the conditions studied. Thermal conductivity $k_t \cong 0.214$ W m^{-2} K^{-1} was independently determined by 'sandwiching' the PVC plate between thick aluminium walls, imposing a known power to an electric heater and measuring the total temperature drop.

In this experiment the heat transfer coefficient and Nusselt number [equations (6) and (7)] was evaluated, as a function of several independent values. Therefore, the effect of the uncertainty in a single measurement on the calculated result would be:

$$\delta R_i = \frac{\delta R}{\delta x_i}\varepsilon_i. \tag{10}$$

When several independent variables are used, which is the case of our interest, we use root root-sum-square (RSS) method [20].

$$\varepsilon_R = \left[\sum_{i=1}^{N}\left(\frac{\partial R}{\partial x_i}\varepsilon_i\right)^2\right]^{1/2} \tag{11}$$

where ε_i is the uncertainty in the generic variable x_i.

On the basis of equation (11), the experimental uncertainty in h can be calculated as:

$$\frac{\varepsilon_h}{h} = \frac{1}{h}\left[\sum_{i=1}^{N}\left(\frac{\partial h}{\partial x_i}\varepsilon_i\right)^2\right]^{1/2}. \tag{12}$$

In equation (12) there are five independent values: the two wall temperatures T_l and T_b, the bulk air temperature T_a, the thermal conductivity of corrugated/undulated plate and liquid crystal package, and thickness of liquid crystal and plate package δ_t. The maximum error of wall temperature (T_l) measurement by the present method is within ± 0.05 (hue range 45–55). The error of the bulk air temperature is

Table 3. Uncertainty analysis for corrugated plate UP1 and $\phi = 30°$

Re	Nu_{av}	$\left(\frac{\partial h}{\partial k_t}\right)\cdot\varepsilon_k$	$\left(\frac{\partial h}{\partial \delta_t}\right)\cdot\varepsilon_\delta$	$\left(\frac{\partial h}{\partial T_b}\right)\cdot\varepsilon_b$	$\left(\frac{\partial h}{\partial T_l}\right)\cdot\varepsilon_l$	$\left(\frac{\partial h}{\partial T_a}\right)\cdot\varepsilon_a$	Average error [%]
1450	11.8	0.696	0.298	12.25	0.92	0.225	±41.0
2030	14.6	1.01	0.43	11.878	0.97	0.329	±27.4
2950	19.4	1.30	0.55	11.59	1.02	0.420	±21.1
10,021	49.7	1.39	1.21	9.94	1.27	0.920	±8.7

$\pm 0.1°C$ and $\pm 0.025°C$ for the water, respectively. The uncertainty of thermal conductivity measurements for plate-liquid crystal package is ± 0.005 W $(mK)^{-1}$. An example of the uncertainty analysis based on equation (12) is given in Table 3. It shows that the uncertainty in average heat transfer coefficient or Nusselt number varies from $\pm 41\%$ (lower Reynolds number) to $\pm 8.7\%$, (higher Reynolds number). Also the uncertainty in the local heat transfer coefficient, h, or Nusselt number, Nu, varies and the largest uncertainties are associated with regions where the temperature difference between the liquid crystal T_l and the water bath T_b is small. Some improvement over the present experimental accuracy could be achieved by increasing the thickness, δ_t, of the corrugated/undulated plate; this, however, would cause the different experimental conditions from real rotary air preheaters [1, 21]. The uncertainty of Reynolds numbers, based on hydraulic diameter of the corrugated/undulated ducts and velocity measurements by hot-wires probe is within $\pm 5\%$ and should not be strictly regarded as an experimental uncertainty since the 'reference' velocity U is calculated from mass flow rate. Finally, minor uncertainties in Re arise from irregularities in the channel spacing and from approximations in the physical properties of air. Of course, uncertainties in U cause corresponding uncertainties in the friction factors, f, defined by equation (9); these can be estimated to be within $\pm 10\%$ under most conditions [2, 5].

DISCUSSIONS AND CONCLUSIONS

The present corrugated–undulated geometry (CU) can be considered as a generalised of the crossed-corrugated geometry studied in previous work [2, 5] and distribution of the local heat transfer coefficient, flow field, and global performance parameters such as Nu_{av} and f, were successfully measured for its heat transfer elements. In particular, the CU geometry is re-examined as a special case by setting identical geometrical parameters H, P, δ, r for the corrugated and undulated ducts. Also in all investigated, the furrows of the *corrugated plates* (CP) were parallel to the main flow direction, while the furrows of the undulated plate were at an angle varying between 20 and 70°. The Reynolds number varied from 1400 to 10,000; however, the range of maximum interest of engineering applications is likely to be Re 1500–3000. As remarked above, six basic configurations have been

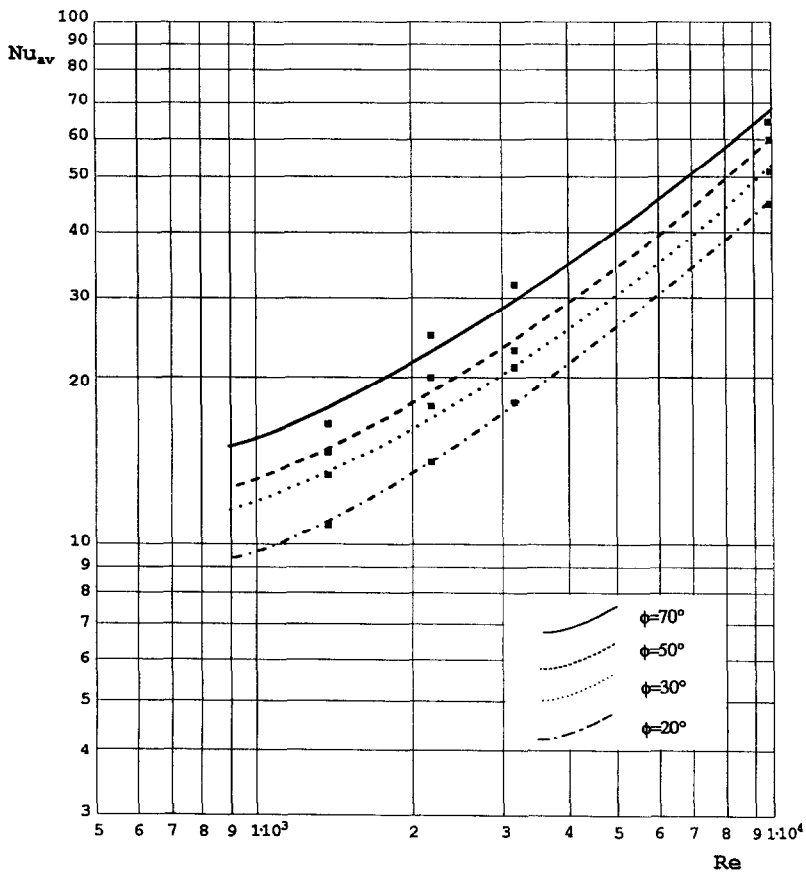

Fig. 6. Average Nusselt number for *corrugated plate* (CP) as a function of Reynolds number for various corrugation–undulation angles of CP/US (CP—$P/H_l = 1.72$; US—$P/H_u = 6.0$; $H_{iu} = 3.65$ mm).

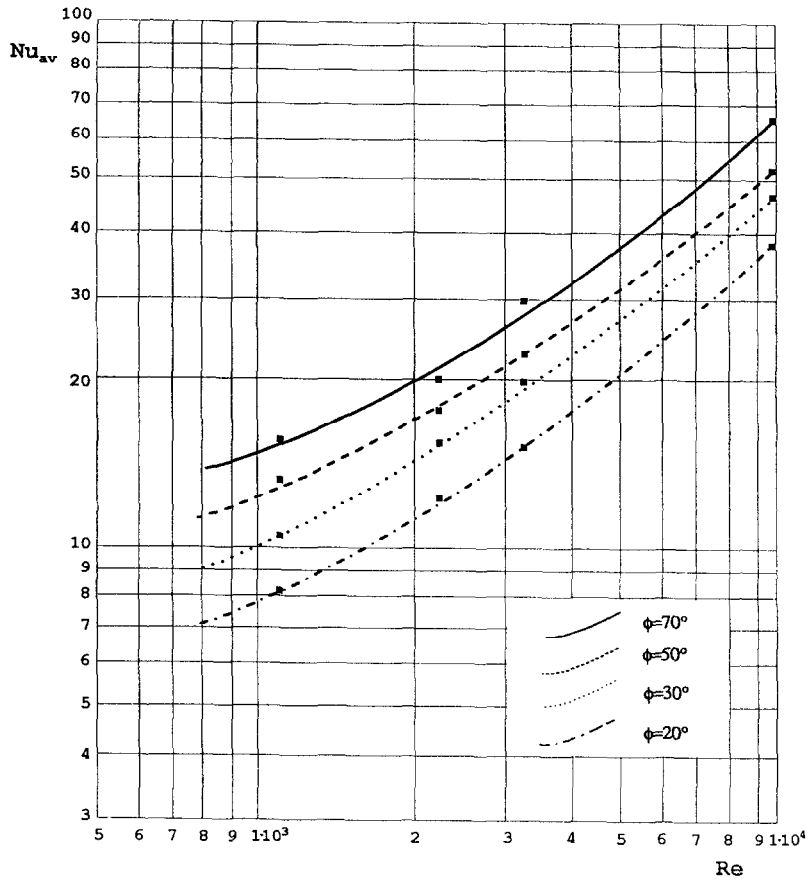

Fig. 7. Average Nusselt number for *undulated plate* (US) as a function of Reynolds number for various corrugation–undulation angles of CP/US (CP—$P/H_i = 1.72$; US—$P/H_u = 6.0$; $H_{iu} = 3.65$ mm).

studied experimentally and their geometrical characteristics are summarised in Table 1 (the dimensions of the CP were constant for all the tests).

Overall heat transfer results

The heat transfer characteristics of the exchanger can be summarised by specifying the two Nusselt numbers Nu_{av} of the corrugated and undulated surface, respectively. They were estimated as surface-weighted mean values of local Nusselt numbers (Nu_{av} and Nu_{av} for one variation). As was agreed, it was rational to investigate thoroughly the flow-field, heat transfer and pressure drop performance for the CU element with current geometry UCS (undulated cross-corrugated standard) [5, 6] and then to study the effect of the following parameters:

(i) angle—ϕ,
(ii) shape factors—'height and pitch' being the basic geometrical parameters,
(iii) Reynolds number.

For shape factors, while in principle both C and U could be independently varied, the C triangular shape shown in Fig. 5 and Table 1 was preferred from consideration of factors fouling of the surfaces. Hence it was resolved to keep the C geometry fixed and vary only the U shape factor. According to recommendations given by Mr P. E. Chew from PowerGen (Power Technology Centre, U.K.), the test programme covers four variations from the standard US: UH1, UH2, UP1 and UP2. However, a total of six test (include UCS) sequences was investigated.

(1) CP/US
(2) CP/UH1
(3) CP/UH2
(4) CP/UP1
(5) CP/UP2
(6) CP/UCS

The first three geometric arrangements have the same internal radius $r = 3.65$ mm, pitch (normal to axis) 21.87 mm, thickness of the plates $\delta_u = 0.87$ mm, liquid crystal package $\delta_l = 0.15$ mm and three different internal heights namely: $H_i = 3.65$ mm for CP/US; 5.2 mm for CP/UH1 and 2.5 mm for CP/UH2. The geometry of cases 4 and 5 (CP/UP1 and CP/UP2) have the same internal height 3.65 mm taken as the standard, but different pitch values $P = 26.2$ mm for UP1 and 17.5 mm for UP2.

Typical average Nusselt number results are presented in Figs 6 and 7; experimental values of Nu_{av}

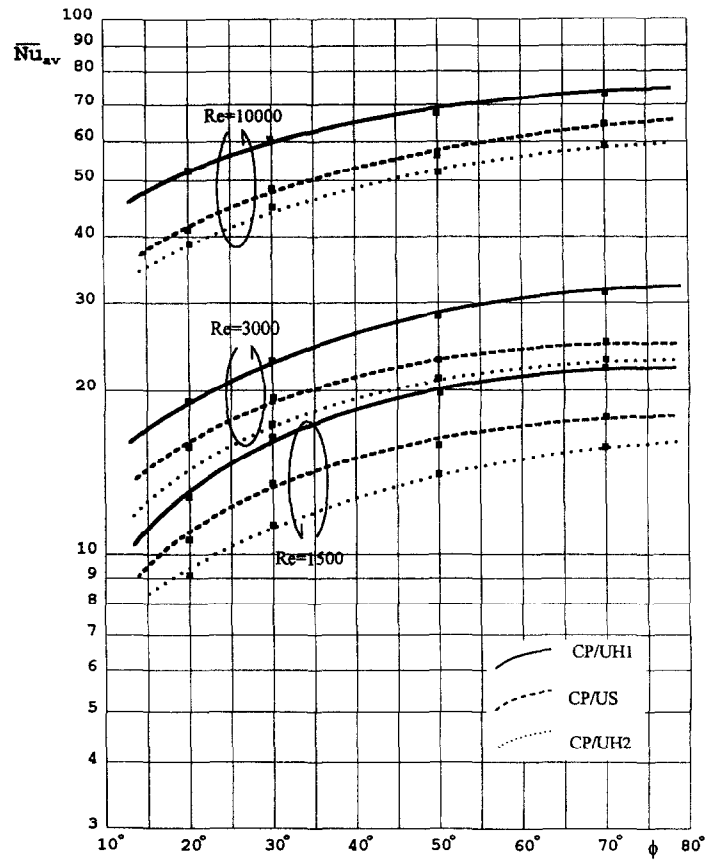

Fig. 8. Equivalent Nusselt number $\overline{Nu}_{av}$ as a function of the undulation angle ϕ (Re = 1500, 3000 and 10,000 for geometries CP/UH1, CP/US and CP/UH2).

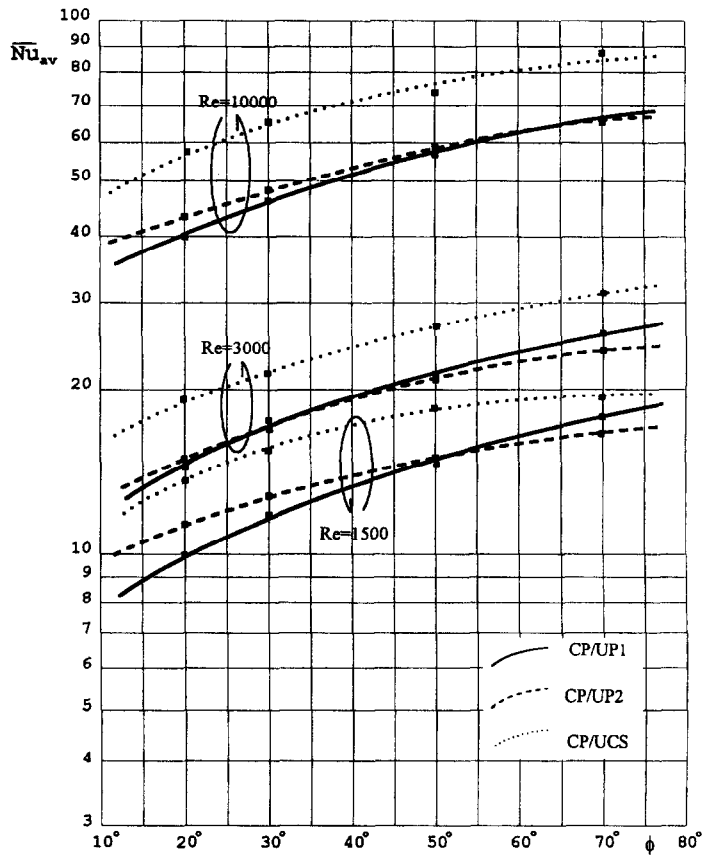

Fig. 9. Equivalent Nusselt number $\overline{Nu}_{av}$ as a function of the undulation angle ϕ (Re = 1500, 3000 and 10,000 for geometries CP/UP1, CP/UP2 and CP/UCS).

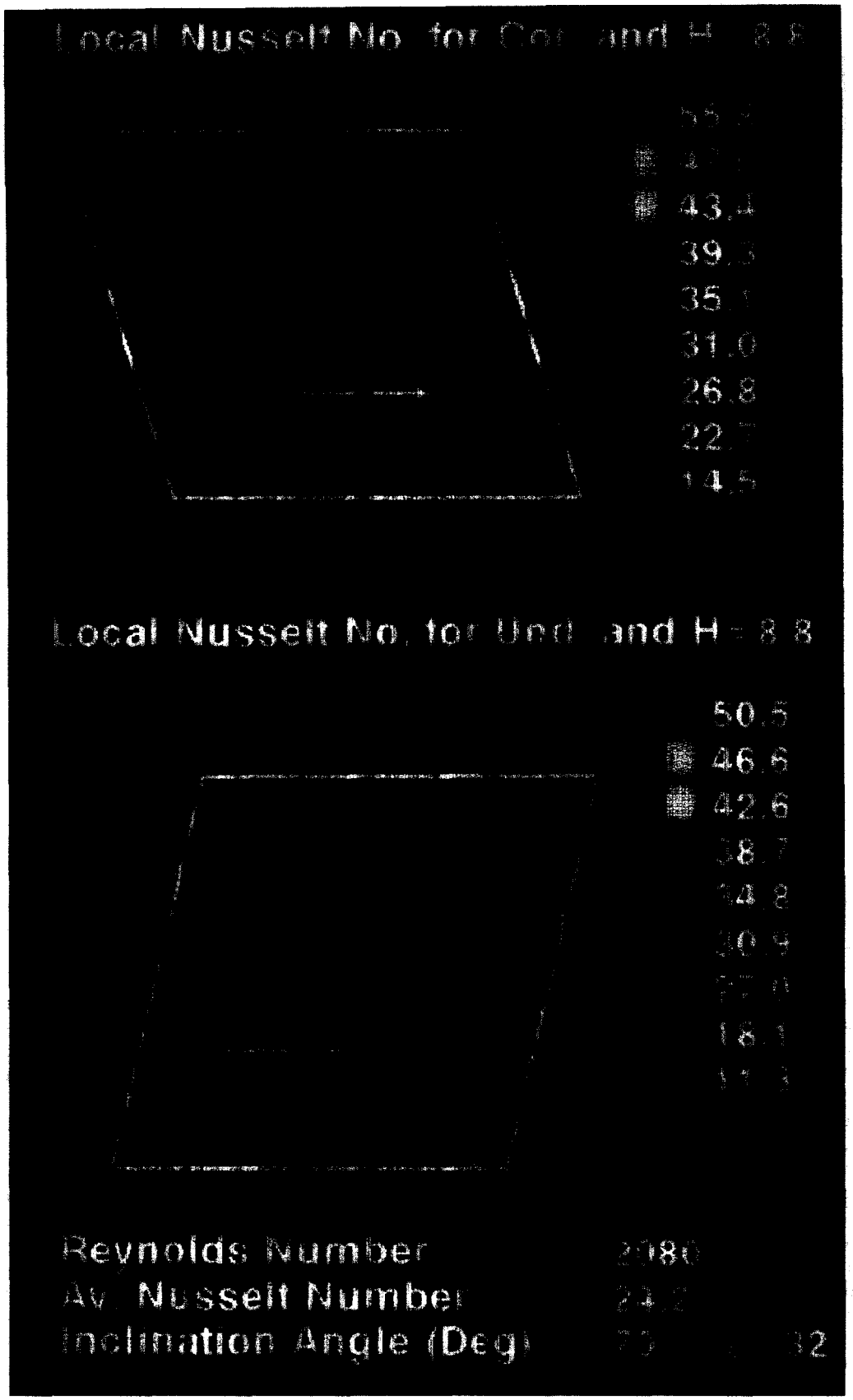

Fig. 10. False colour image of local Nusselt number contours over a central diamond of the corrugated and undulated plated CP/UCS ($\phi = 70°$, $Re = 2080$; $H = 8.8$ mm).

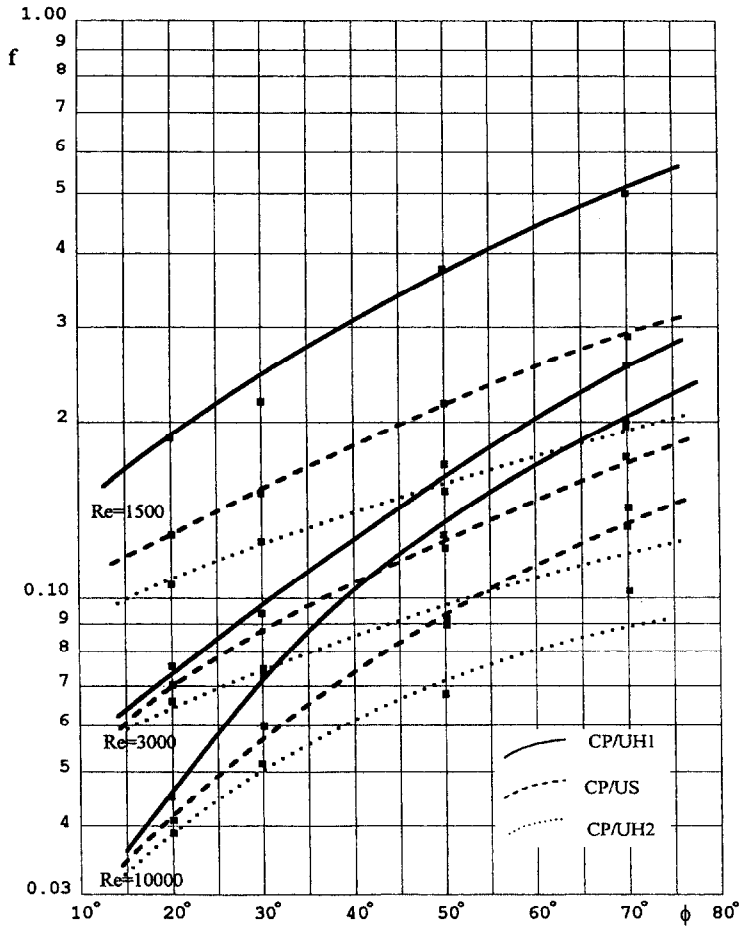

Fig. 11. Equivalent friction coefficient f as a function of the undulation angle (Re = 1500, 3000 and 10,000 for geometries CP/US, CP/UH1 and CP/UH2).

are reported as a function of Reynolds number for various corrugated–undulation angles of CP/US geometry. It can be observed that, when ϕ increases from 20 to 70°, Nu_{av} increases by about 80–90%, i.e. much less than the friction coefficient (which increases by almost 3–4 times).

The overall heat transfer results are evidence in Figs 8 and 9: experimental values of Nu_{av} are reported for six geometries and for Re = 1500, 3000 and 10,000. There is a significant (~50%) increase in the Nusselt number when the ratio H_u/H_c increases from 0.24 (geometry UH2) to 0.43 (geometry UH1). Interestingly enough, the increase in the undulation depth causes Nu to increase by about the same amount on *both* the corrugated and undulated plates. In contrast, when the aspect ratio P/H increases from 3.87 (geometry UP2) to 5.8 (geometry UP1), at *a constant* value of H_i (3.65 mm), the Nusselt number varies by approximately 5% which is comparable to the order of magnitude of the experimental error.

Distribution of the local heat transfer coefficient

The distribution of the local heat transfer coefficient, expressed as a Nusselt number Nu, is shown in Fig. 10 for some representative test cases. The colour scale represent the various video images of the Nusselt number distribution are joined into a single image using the Global Lab software of Data Translation Inc. [2]. This shows the Nusselt number distribution on the central diamond of the CU working section. Maxima of Nu are attained near the downstream end of the trailing edge and as expected, maxima of Nu are located around the four corners where the top plate touches the bottom one. Values of Nu are also high in the impingement regions, which correspond to a restriction in the available cross-sectional flow area (flow contraction). As previously observed [2, 5] in the case of crossed corrugated geometry, maxima are shifted markedly downstream along the main flow direction and inclination angle ϕ. In the whole central (furrow) region levels of Nu are low. This shows that this region contributes little to overall heat transfer. However, in this experimental condition, by increasing the depth of the furrows, the average heat transfer coefficient is increased. It is evident from Figs 8 and 9, that for identical dimensionless parameters, but different geometry, the Nusselt number is almost identical (CP/UH1 and CP/UCS).

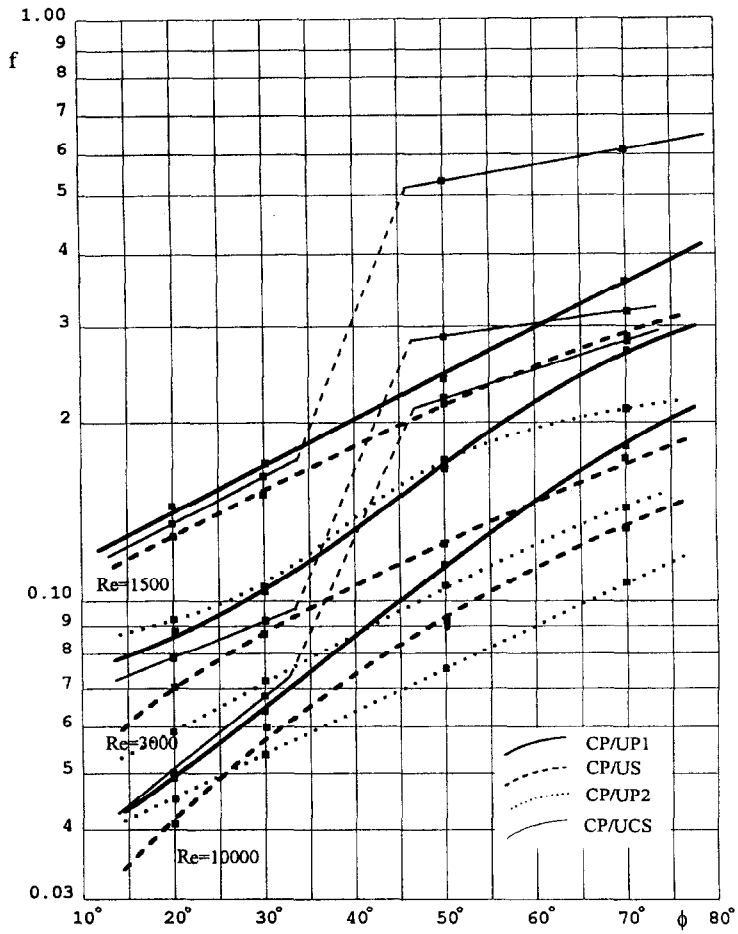

Fig. 12. Equivalent friction coefficient f as a function of the undulation angle (Re = 1500, 3000 and 10,000 for geometries CP/US, CP/UP1, CP/UP2 and CP/UCS).

Pressure drop

The experimental results of pressure drop are presented in Figs 11 and 12, in the form of the friction coefficient f as a function of the undulation angle ϕ and three Re (1500, 3000 and 10,000). The influence of the angle on the friction coefficient is much larger than on the Nusselt number. The dependence of f on the pitch-to-height is difficult to separate from the influence of ϕ and Re and is less easy to interpret than that of the Nusselt number.

The dependence of f on ϕ can be crudely approximated at all Reynolds number and pitch to height ratios by a simple exponential low:

$$f \cong a\, Re^{-b} \tag{13}$$

provided that the exponent b is made to vary from 1.28 to 0.193 (Table 2).

The geometry, inclination angle ϕ, boundary conditions and Reynolds number Re all have a significant effect on the pressure drop or fraction coefficient f. As the depth of undulation furrows increases (from UH2 to US and UH1), the friction coefficient f becomes significantly larger. Probably the intensity of secondary motion increases and the contraction edges become steeper. From Fig. 12 we find that the height (CP/UP2, CP/US and CP/UP1) has less influence on the Nusselt number and friction coefficient distribution.

Boundary effects

The values of Nu and f reported and discussed above are all for the condition of *close side boundaries* of the working section. The main effect of closing the sides is a moderate decrease of the friction factor and Nusselt number of the highest inclination angle (more than 45°). For values ϕ less than 45° and a smaller aspect ratio P/H_i (CP/UCS), the flow field or pattern flow essentially change-close working section becomes an open one without 'reflection'.

Finally, in this paper the effect of inclination angle, geometry and Reynolds number have all been investigated. This is with a view to optimise the design, as used in the very large rotary regenerators of conventional fossil fuel fire steam power plants. However, the results are of more general interest to compact heat exchanger design. Also, it was found that the

inclination angle ϕ is a major parameter which influences the performance of plate heat exchanger. This is because a change in ϕ effects the basic flow structure which is primary factor affecting pressure drop and heat transfer.

Acknowledgements—The author wishes to thank the Science and Engineering Research Council together with PowerGen U.K. and Nat Power plc who jointly funded the work described in this paper under the ERCOS scheme. I would also like to extend my grateful thanks to my colleagues, Professors I.K. Smith and M.W. Collins, for their encouragement and help during my stay at City University. The financial assistance of the National Committee of Fundamental Research (KBN), Poland within the Grant no. 8 T10B 060 12 is gratefully acknowledged.

REFERENCES

1. Chew, P. E., Rotary air preheaters on power station boilers. *Proceedings of the Symposium on Waste Heat Recovery and Utilisation*, Institute of Energy, U.K., 1985.
2. Stasiek, J., Smith, I., Shand, A., Ciofalo, M., Chew, P. and Collins, M. W., Local heat transfer and fluid flow fields in crossed corrugated geometrical elements for rotary heat exchangers. Report nos 1–13. Thermofluids Engineering Research Centre, City University, London, 1989–1994.
3. Burns, A. D., Jones, I. P., Kightley, J. R. and Wilkes, N. S., Harwell—FLOW3D, Release 2.1 : User Manual. Report AERE-R (Draft), Harwell, U.K., 1988.
4. Stasiek, J., Collins, M. W. and Chew, P. E., Liquid crystal mapping of local heat transfer in crossed corrugated geometrical elements for air heat exchangers. *Proceedings of the EUROTECH-Direct'91—Thermofluid Engineering*, IMCHE, U.K. 1991.
5. Stasiek, J., Collins, M. W., Ciofalo, M. and Chew, P. E., Investigation of flow and heat transfer in corrugated passages—I. Experimental results. *International Journal of Heat and Mass Transfer*, 1996, **39,** 142–164.
6. Ciofalo, M., Stasiek, J., Collins, M. W. and Chew, P. E., Investigation of flow and heat transfer in corrugated passages—II. Numerical simulations. *International Journal of Heat and Mass Transfer*, 1996, **39,** 165–192.
7. Data Translation Inc., *Image Processing Handbook*, 1991.
8. Reinitzer, R., Beitrage zur Kenntniss des Cholestrins, Monatschr. *Chemie Wien*, 1888, **9,** 421–441.
9. Brown, G. M. and Shaw, W. G., The mesomorphic state : liquid crystals. *Chemistry Review*, 1957, **57,** 1049–1157.
10. Fergason, J. L., Liquid crystal in nondestructive testing. *Applied Optics*, 1968, **7,** 1729–1737.
11. Stephen, M. J. and Straley, J. P., Physics of liquid crystals. *Review of Modern Physics*, 1974, **46**(4), 617–704.
12. Jones, T. V., Wang, Z. and Ireland, P. T., The use of liquid crystals in aerodynamic and heat transfer experiments. *Proceedings of the Optical Methods and Data Processing in Heat and Fluid Flow*, City University, London, 1992, pp. 51–65.
13. Parsley, M., The use of thermochromic crystals in heat transfer and flow visualisation research. *FLUCOME'88*, Sheffield University, U.K., 1988, pp. 216–220.
14. Merck Limited, Poole, Dorset, U.K., *Thermochromic Liquid Crystals Manufacturer's Catalogue*, 1994.
15. Hallcrest Products, Glenview, IL, U.S.A., *The HALLCREST Handbook of Thermochromic Liquid Crystal Technology*, Manufacturer's catalogue, 1995.
16. Akino, N., Kunugi, T., Ichimiya, K., Mitsushiro, K. and Ueda, M., Improved liquid crystal thermometry excluding human color sensation. *Journal of Heat Transfer*, 1989, **11,** 558–565.
17. Moffat, R. J., Experimental heat transfer. *Proceedings of the 9th International Heat Transfer Conference*, Jerusalem, Vol. 1, 1991, pp. 308–310.
18. Hollingsworth, D. K., Boehman, A. L., Smith, E. G. and Moffat, R. J., Measurement of temperature and heat transfer coefficient distributions in a complex flow using liquid crystal thermography and true-colour image processing. *ASIME Heat Transfer*, 1989, **123,** 35–42.
19. Goldstein, R. J. and Franchett, M. E., Heat transfer from a flat surface to an oblique impinging jet. *Journal of Heat Transfer*, 1988, **110,** 84–90.
20. Moffat, R. J., Describing the uncertainties in experimental results. *Experimental Thermal and Fluid Sciences*, 1988, **1,** 3–17.
21. Chojnowski, B. and Chew, P. E., Getting the best out of rotary air heaters. *CEGB Research Journal*, 1978, 14–21.